PNAS RESEARCH ARTICLE | BIOCHEMISTRY OPEN ACCESS

Direct activation of SARM1 by dsDNA is not supported by biochemical and cellular evidence

Allison H. Kao[a,b,1], Biswa P. Mishra[c,1], Mitchell Sorbello[d,1], Wenbin Zhang[e,1], Qinyi Zhou[e], Yuefeng Jiang[f], Veronika Masic[c], Paige Harten[c], Weixi Gu[d], Jian Yuan Yang[g], A. Joseph Bloom[b,h], Robi D. Mitra[b,2], Zhe Zhang[f,2], Yong Juan Zhao[g,2], Giuseppe Orsomando[i,2], Xiaodong Wang[e,2], Jeffrey Milbrandt[b,h,2], Bostjan Kobe[d,2], Thomas Ve[c,2], and Aaron DiAntonio[a,h,2]

Affiliations are included on p. 11.

Contributed by Xiaodong Wang; received June 14, 2026; accepted August 5, 2026; reviewed by Casper Hoogenraad and Thomas L. Schwarz

Sterile alpha and Toll/interleukin-1 receptor motif–containing protein 1 (SARM1) is a NAD$^+$-consuming enzyme that drives axon degeneration and is activated by changes in the NMN/NAD$^+$ ratio. A recent study proposed that cytosolic double-stranded DNA (dsDNA) directly binds SARM1's TIR domain, activating it independently of this canonical mechanism. Here, we evaluate dsDNA-dependent SARM1 activation using purified SARM1, biochemical and biophysical assays, primary neurons, and cellular pharmacology. Across multiple platforms, dsDNA does not stimulate SARM1 NADase activity, promote higher-order assembly, or generate the metabolic signature of activated SARM1. When effects are observed, they are weak, context-dependent, and inconsistent across assays, and do not support a defined activation mechanism. In cells, dsDNA induces NAD$^+$ depletion through PARP-dependent pathways independently of SARM1. The reported DNA-binding mutant (3KE-SARM1) is nonfunctional in canonical SARM1 activation paradigms such as axotomy and therefore cannot be used to infer dsDNA activation mechanisms. Together, these findings do not support a model in which SARM1 is directly activated by dsDNA.

SARM1 | NADase | axon degeneration | DNA | neurodegeneration

Significance

Sterile alpha and Toll/interleukin-1 receptor motif–containing protein 1 (SARM1) activation is sufficient to trigger the genetic axon degeneration program, making its upstream regulatory mechanisms a major focus of neurodegeneration research and therapeutic development. A recent study proposed that double-stranded DNA directly activates SARM1 through a mechanism distinct from its established role as a sensor of metabolic stress. Across multiple independent laboratories and orthogonal experimental systems, we find no evidence that DNA directly activates SARM1. Instead, DNA-induced NAD$^+$ depletion in cells is mediated by PARP enzymes independently of SARM1. By distinguishing DNA-triggered metabolic stress from direct SARM1 activation, this work clarifies a central mechanism of axon degeneration and provides a framework for interpreting SARM1-dependent and SARM1-independent NAD$^+$ depletion pathways.

Sterile alpha and Toll/interleukin-1 receptor motif–containing protein 1 (SARM1) is a central executioner of axon degeneration and an inducible NAD$^+$-consuming enzyme whose activation precipitates energetic collapse (1–6). In neurons, SARM1 is activated downstream of axonal injury, NMNAT2 loss, and exposure to NMN mimetics CZ-48 or toxins such as vacor and 3-AP, resulting in rapid NAD$^+$ depletion and axon fragmentation (7–10). Early genetic and biochemical studies established that accumulation of nicotinamide mononucleotide (NMN) is a key driver of axon degeneration (11), and subsequent structural and mechanistic work defined SARM1 as a metabolic sensor of the NMN/NAD$^+$ ratio (12–15). In its basal state, SARM1 is maintained in an autoinhibited conformation through interactions involving the N-terminal ARM domain (16). Binding of NAD$^+$ to an allosteric pocket within the ARM domain prevents NMN binding, whereas accumulation of NMN competitively displaces NAD$^+$, relieving autoinhibition and permitting assembly of the TIR domains into a catalytically active NADase complex (12, 17). Thus, SARM1 activation is governed by shifts in the NMN/NAD$^+$ ratio, which serve as the proximal trigger for enzymatic activity. Recent structural and biochemical studies have expanded the canonical NMN/NAD$^+$ allosteric model of SARM1 activation by demonstrating that other mechanisms can promote SARM1 activation, such as by identifying intermediate conformational states and multistep transitions that precede full NADase engagement (18–20).

This metabolic model provides a unifying framework for diverse degenerative stimuli. Axotomy leads to rapid depletion of NMNAT2 and accumulation of NMN in the axon distal to the cut, shifting the NMN/NAD$^+$ ratio and activating SARM1 (11, 12, 21). Similarly, vacor and 3-AP are metabolized to NMN analogs that engage the same allosteric site and promote activation (9, 10). In these contexts, SARM1 activity can be blocked by genetic deletion or pharmacologic inhibition, preventing NAD$^+$ depletion and axon degeneration. Together, these findings position SARM1 as a sensor of intracellular metabolic state rather than a direct receptor for upstream stress signals (22, 23).

Beyond acute injury, SARM1 has been implicated in a broad range of neurodegenerative conditions, including peripheral neuropathies, chemotherapy-induced neuropathy, traumatic brain injury, and glaucoma (24–27). Small-molecule SARM1 inhibitors have been developed, and clinical evaluation of SARM1-targeted therapies is underway (14, 15, 28–32). Because therapeutic strategies aim to modulate SARM1 activity in patients,

Copyright © 2026 the Author(s). Published by PNAS. This open access article is distributed under Creative Commons Attribution-NonCommercial-NoDerivatives License 4.0 (CC BY-NC-ND).

[1]A.H.K., B.P.M., M.S., and W.Z. contributed equally to this work.

[2]To whom correspondence may be addressed. Email: rmitra@wustl.edu, zzhang01@pku.edu.cn, zhaoyongjuan@cuhk.edu.cn, g.orsomando@staff.univpm.it, wangxiaodong@nibs.ac.cn, jmilbrandt@wustl.edu, b.kobe@uq.edu.au, t.ve@griffith.edu.au, or diantonio@wustl.edu.

This article contains supporting information online at https://www.pnas.org/lookup/suppl/doi:10.1073/pnas.2620112123/-/DCSupplemental.

Published September 11, 2026.

Downloaded from https://www.pnas.org by 151.76.23.94 on September 13, 2026 from IP address 151.76.23.94.

a precise understanding of the molecular mechanisms governing its activation is essential.

A recent study by Wang et al. (33) proposes a distinct novel mechanism of SARM1 activation in which cytosolic double-stranded DNA (dsDNA) directly binds to basic residues within the TIR domain (33). In this model, dsDNA promotes TIR oligomerization and NAD^+ cleavage independently of the canonical NMN/NAD^+ allosteric mechanism. The authors further report that substitution of three conserved lysines in the TIR domain (K602E/K628E/K636E; "3KE") selectively impairs dsDNA-dependent activation while preserving responsiveness to NMN-mimetic stimulation, suggesting that SARM1 functions as a direct dsDNA sensor. Because this mechanism substantially expands the conceptual framework of SARM1 activation beyond metabolic sensing, independent evaluation of dsDNA-dependent activation is important.

Here, we comprehensively evaluate the model that SARM1 is directly activated by dsDNA. Using mammalian cell-expressed full-length human SARM1, we assess NADase activity and higher-order assembly under conditions reported to support dsDNA-dependent activation across orthogonal assays and independent laboratories. Across these systems, dsDNA does not stimulate SARM1 NADase activity or promote higher-order assembly under conditions in which canonical NMN-dependent activation is robustly detected. While weak, context-dependent effects can be observed under limited conditions, these signals are not reproducible across assays, depend strongly on nucleic acid length, preparation, and purity, and do not exhibit the defining features of canonical NMN-mediated activation. In cellular systems, dsDNA transfection induces NAD^+ depletion and loss of viability, but these effects are PARP-dependent and occur independently of SARM1. We therefore reexamine the SARM1 TIR domain mutant 3KE, which was proposed to selectively disrupt DNA-dependent activation, and find that it behaves as a loss-of-function allele and lacks NADase activity in canonical NMN-dependent paradigms such as axonal injury. Together, these findings do not support a model in which SARM1 functions as a dsDNA sensor and instead reinforce the currently accepted framework in which SARM1 activation is governed by metabolic state.

Results

dsDNA Does Not Activate or Oligomerize Purified SARM1 in a Reproducible or Mechanistically Defined Manner. To assess whether nucleic acids directly activate SARM1, we examined purified human SARM1 using orthogonal biochemical assays performed in five independent laboratories, including NMR-, HPLC-, fluorescence-, and LC–MS-based readouts of catalytic activity and product formation (Fig. 1*A*). Full-length human SARM1 (hereafter SARM1; residues 1 to 724), human SARM1 lacking the mitochondrial targeting sequence (hereafter ΔN-SARM1; residues 28 to 724), a construct previously shown to retain full degenerative function after neuronal reexpression (34) while facilitating biochemical analysis, and the isolated SARM1 TIR-domain (hereafter $SARM1^{TIR}$), which possesses all reported dsDNA binding residues (33), were expressed and purified from mammalian or bacterial cells, as described previously (4, 15). NADase activity was first quantified using a ^1H NMR-based assay, which enables direct measurement of NAD^+ consumption and product formation. As expected, addition of NMN robustly stimulated cleavage of NAD^+, validating enzyme integrity and assay sensitivity (Fig. 1*B*). In contrast, incubation of ΔN-SARM1 with a 90-bp dsDNA fragment identical to that used by Wang et al. (33) did not increase NADase activity above baseline or produced no measurable stimulation at either NAD^+ concentration tested (500 μM or 2 mM) (Fig. 1*B* and *SI Appendix*, Fig. S1 *A* and *B*). Similar results were obtained with single-stranded DNA (ssDNA) of comparable length and composition (Fig. 1*C* and *SI Appendix*, Fig. S1 *C* and *D*) and $SARM1^{TIR}$ (*SI Appendix*, Fig. S1*E*). Because dsDNA has been proposed to activate SARM1 by binding to and promoting clustering of the TIR domains, we next tested whether nucleic acid–mediated activation requires the NMN-induced conformational change that relieves autoinhibition and exposes the TIR domains. Under these conditions, NMN robustly activated SARM1 as expected; however, addition of dsDNA or ssDNA did not further enhance NMN-induced activity. These results indicate that nucleic acids do not potentiate SARM1 activation, even when the enzyme is in the NMN-activated state (Fig. 1 *B* and *C*).

To directly assess reaction products using a more sensitive assay, purified SARM1 incubated with NAD^+ was analyzed by targeted LC–MS/MS following incubation with NMN or dsDNA. NMN induced robust NAD^+ consumption and production of ADPR and cADPR, consistent with the established profile of activated SARM1 (3, 5, 35). In contrast, none of the dsDNA ligands tested altered NAD^+, ADPR, or cADPR levels relative to control reactions, indicating that dsDNA does not trigger catalytic turnover or product formation in direct measurements of NAD^+ metabolism (Fig. 1 *D–F* and *SI Appendix*, Fig. S2 *A* and *B*).

Consistent results were obtained using independently purified SARM1 preparations in two additional assay systems, HPLC and the fluorescent reporter PC6 (36). While PC6 provides a sensitive fluorescence-based readout of the SARM1 base exchange reaction, it is an indirect assay and therefore complements, but does not supersede, direct measurements of NAD^+ turnover. Across these platforms, including inducible SARM1 preparations tested under the assay conditions reported by Wang et al. (33), we did not detect reproducible activation by linear dsDNA fragments of varying lengths or compositions, whereas NMN robustly activated SARM1 under all conditions tested (Fig. 1 *G–I* and *SI Appendix*, Fig. S2 *C* and *D*). The nucleic acid substrate poly(dA:dT), a well-known experimental ligand of cytosolic dsDNA sensors, also did not activate SARM1. To rule out an inhibitory component in our dsDNA preparations, we coincubated SARM1 with dsDNA and NMN, but we again found that its activation kinetics were unaffected by dsDNA coincubation (*SI Appendix*, Fig. S2*E*).

Notably, a large circular plasmid DNA (>10 kb) produced a small but statistically significant increase in activity in one assay configuration, whereas shorter linear dsDNA fragments (≤90 bp) remained inactive under the same conditions (Fig. 1*I*). However, this effect was substantially weaker than NMN-induced activation and did not approach the level of canonical activation. Its restriction to very large DNA species indicates that it does not reflect a defined ligand interaction, but rather a nonspecific property of highly extended nucleic acids.

In an independent fluorescence-based PC6 assay using a 125-bp dsDNA fragment of fixed sequence, we observed marked preparation-dependent variability. Four independently generated in-house PCR-derived preparations of this fragment did not increase SARM1 activity, whereas two commercially synthesized preparations of the same sequence showed discordant behavior, with one exhibiting weak stimulation and the other substantially greater activity. Notably, the strongest apparent activation was markedly reduced following sodium acetate–ethanol precipitation, indicating that the effect is not a property of the dsDNA itself, but rather due to a contaminant in the preparation (*SI Appendix*, Fig. S2 *F–H*). This effect may be related to the ability of molecular crowding agents, such as polyethylene glycol and citrate, to

Downloaded from https://www.pnas.org by 151.76.23.94 on September 13, 2026 from IP address 151.76.23.94.

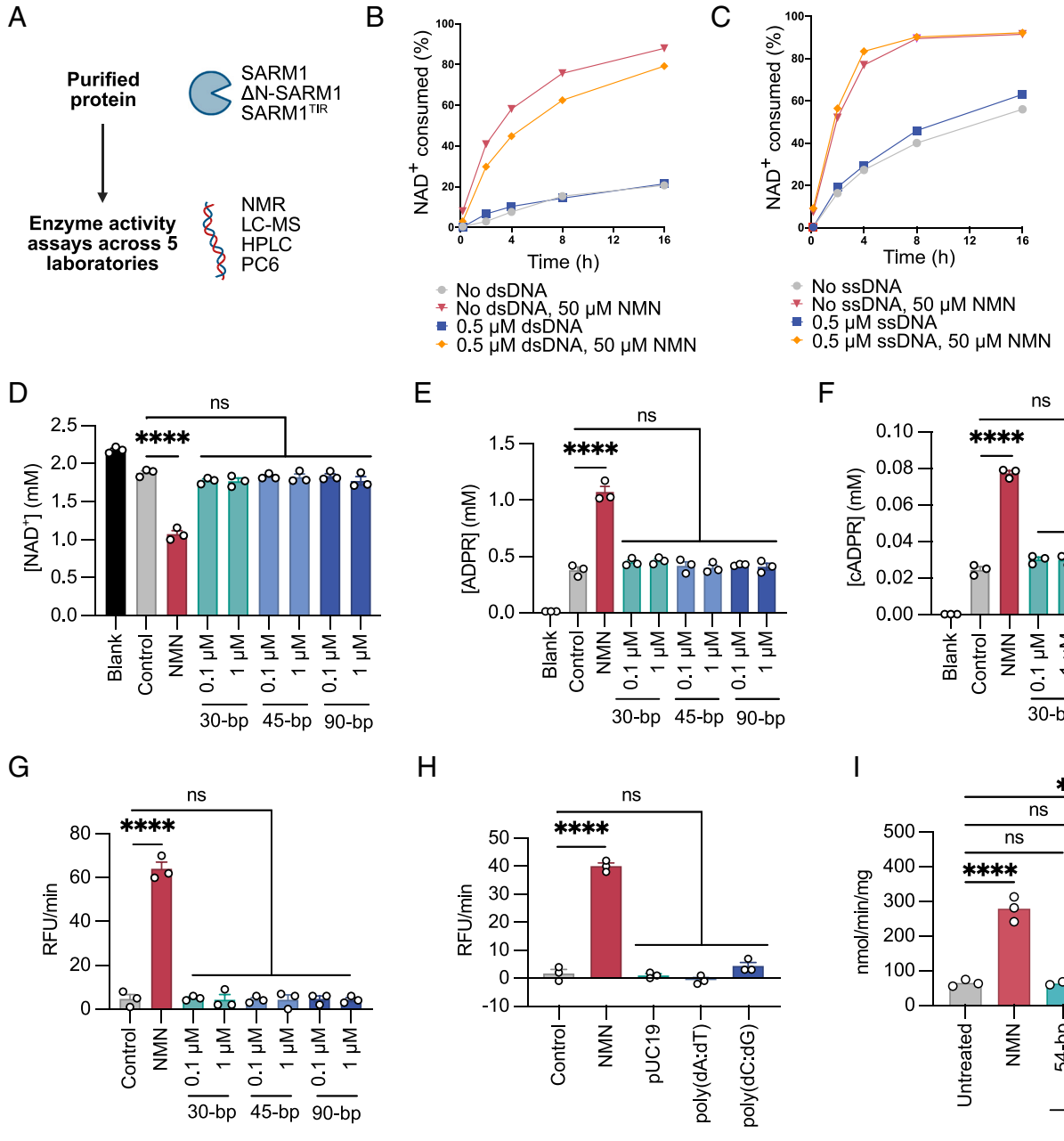

Fig. 1. Orthogonal biochemical assays across five laboratories fail to detect SARM1 activation by dsDNA in vitro. (*A*) Models and assays of SARM1 enzymatic activation by dsDNA used in this study. (*B* and *C*) NMR reaction progress curves for purified human SARM1 lacking the mitochondrial targeting sequence (ΔN-SARM1; 0.5 μM) incubated with 0.5 μM 90-bp dsDNA (*B*) or ssDNA (*C*) and/or NMN (50 μM). Reactions were initiated with NAD^+ (500 μM), and NAD^+ consumption was quantified over time. One representative experiment is shown, and additional replicates are provided in *SI Appendix*, Fig. S1 ($n = 3$ biological replicates). (*D–F*) Targeted LC–MS/MS quantification of NAD^+ (*D*), ADPR (*E*), and cADPR (*F*) following incubation of purified full-length SARM1 (0.1 μM) with NMN (1 mM) or dsDNA (0.1 or 1 μM) for 60 min after addition of NAD^+ (2 mM). NMN induced NAD^+ consumption with production of ADPR as the dominant product and lower levels of cADPR, whereas dsDNA did not alter NAD^+, ADPR, or cADPR ($n = 3$ biological replicates). (*G* and *H*) Fluorescence-based PC6 reporter assay measured in Relative Fluorescent Units (RFU)/min for purified full-length SARM1 (0.1 μM), showing robust activation with NMN (1 mM) but not the indicated dsDNA substrates ($n = 3$ biological replicates). (*I*) HPLC-based quantification of NAD^+ consumption, expressed as fold-activation relative to untreated control (defined in *Materials and Methods*) using soluble preparations of ΔN-SARM1 incubated with dsDNA (0.2 μM, 54- or 81-bp; 0.05 μM, 10,853-bp) or NMN (0.5 mM) for 60 min after the addition of NAD^+ (2 mM) ($n = 3$ biological replicates). For (*B* and *C*), traces show one representative protein preparation. For (*D–I*), data are mean ± SEM. A one-way ANOVA with Dunnett's multiple-comparisons test was performed comparing each experimental condition to the control (*D–H*) or untreated (*I*) condition. $^*P < 0.05$; $^{**}P < 0.01$; $^{***}P < 0.001$; $^{****}P < 0.0001$; n.s., not significant.

influence activation of isolated SARM1 TIR domains (18). Together, these findings indicate that any apparent dsDNA-dependent signal is weak, not reproducible across assays, and highly sensitive to DNA preparation.

Because the limited effects observed in these experiments lacked the defining features of canonical SARM1 activation, we therefore assessed whether nucleic acids physically associate with SARM1 or promote higher-order assembly as proposed by Wang et al. (33) using complementary biochemical and biophysical approaches. Electrophoretic mobility shift assays using 5′-Cy5-labeled dsDNA fragments ranging from 30 to 300 bp did not detect binding to either SARM1 or $SARM1^{TIR}$ across a broad range of protein concentrations (Fig. 2 *A* and *B* and *SI Appendix*, Fig. S3 *A* and *B*). Consistent with these findings, mass photometry of ΔN-SARM1 incubated with equimolar dsDNA or ssDNA did not reveal formation of binary complexes or higher-order oligomeric species

Downloaded from https://www.pnas.org by 151.76.23.94 on September 13, 2026 from IP address 151.76.23.94.

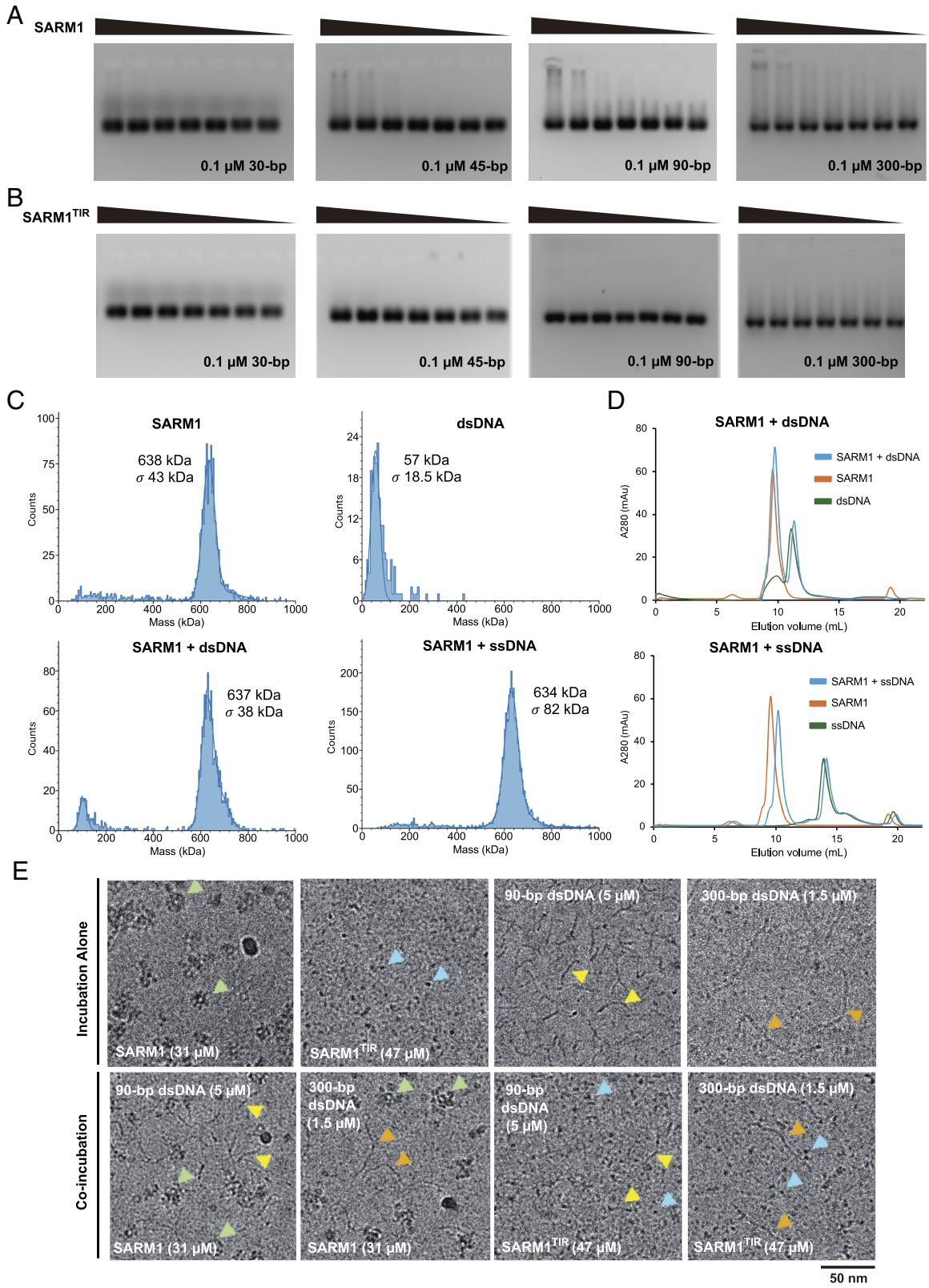

Fig. 2. dsDNA does not detectably bind or promote higher-order oligomerization of SARM1 in vitro. (*A* and *B*) Representative electrophoretic mobility shift assays (EMSA) to assess the binding of purified full-length human SARM1 protein (SARM1; *A*) or the isolated TIR domain (SARM1^{TIR}; *B*) to 5′-Cy5-labeled dsDNA (0.1 μM) of the indicated lengths incubated with protein in a range of concentrations (30 to 0 μM), showing no clear mobility shift under these conditions (n = 3 biological replicates). (*C*) Representative mass photometry results of purified human SARM1 lacking the mitochondrial targeting sequence (ΔN-SARM1, 50 nM) incubated alone or with dsDNA (50 nM) or ssDNA (50 nM), showing similar mass distributions without evidence of nucleic acid-induced higher-order assembly (n = 3 biological replicates). (*D*) Representative size-exclusion chromatography (SEC) of ΔN-SARM1 (10 μM) incubated with dsDNA (2 μM) and ssDNA (2 μM). Overlaid traces show no earlier eluting SARM1 peaks under either condition (n = 2 biological replicates). (*E*) Representative cryo-EM images of SARM1 (31 μM) or SARM1^{TIR} (47 μM) incubated alone or with dsDNA of the indicated length and concentration (90-bp dsDNA, 5 μM; 300-bp dsDNA, 1.5 μM). Arrowheads indicate SARM1 (green), SARM1^{TIR} (blue), 90-bp dsDNA (yellow), and 300-bp dsDNA (orange) (n = 3 biological replicates). For (*A*–*E*), one representative experiment from two or three independent protein preparations is shown; additional preparations for (*C* and *D*) are shown in *SI Appendix*, Fig. S2.

Downloaded from https://www.pnas.org by 151.76.23.94 on September 13, 2026 from IP address 151.76.23.94.

beyond those observed for ΔN-SARM1 alone (Fig. 2*C* and *SI Appendix*, Fig. S3 *C* and *D*). Analytical size-exclusion chromatography likewise showed no earlier-eluting ΔN-SARM1 peaks indicative of multimerization following coincubation with dsDNA or ssDNA (Fig. 2*D* and *SI Appendix*, Fig. S3 *E–I*). Across these orthogonal approaches, we do not detect stable or stoichiometric binding of nucleic acids to SARM1.

As an orthogonal and more sensitive approach, we examined $SARM1^{TIR}$ interactions with a 128-bp dsDNA fragment using microscale thermophoresis (MST). A weak, high-concentration signal was detected, with an apparent transition occurring only at elevated protein concentrations (EC50 ~40 μM) and exhibiting nonhyperbolic, Hill-like behavior inconsistent with a simple 1:1 binding model (*SI Appendix*, Fig. S3 *J* and *K*). No interaction was detected at protein concentrations corresponding to those used in biochemical activity assays. To determine whether this signal reflects DNA-induced assembly as proposed by Wang et al. (33), we performed negative-stain EM under conditions corresponding to both low and high MST signal. No filamentous or higher-order structures were observed at either concentration, and particle distributions were indistinguishable in the presence and absence of DNA (*SI Appendix*, Fig. S4 *A* and *B*). These findings indicate that the MST signal reflects a weak, concentration-dependent interaction that is not coupled to higher-order assembly and is incompatible with a model of DNA-driven filament formation.

We next examined these reactions by cryoelectron microscopy, under conditions spanning the DNA lengths and concentrations reported by Wang et al. (33) to induce SARM1 assembly. Neither SARM1 nor $SARM1^{TIR}$ formed filaments or clustered structures in the presence of 90-bp or 300-bp dsDNA, and nucleic acid species remained spatially separated from protein particles in the imaged fields (Fig. 2*E*). Consistent findings were obtained in an independent negative-stain imaging series using complementary conditions, in which neither full-length SARM1 nor the isolated TIR-domain formed higher-order assemblies in response to nucleic acids (*SI Appendix*, Fig. S4 *C–E*). As a positive control, the DNA-binding plant TIR domain protein L6 formed DNA-induced filaments (37) under identical buffer conditions (*SI Appendix*, Fig. S4*F*), demonstrating that the assay readily detects nucleic-acid-driven assembly when it occurs. Together, these data directly contrast with the assembly model proposed by Wang et al. (33) and do not support nucleic-acid-induced oligomerization of SARM1 in vitro.

Taken together with the biochemical activity measurements, these findings establish a clear hierarchy of effects. Canonical activation by NMN produces robust, reproducible increases in NADase activity across all assay platforms. In contrast, nucleic acids do not stimulate activity across assays and experimental preparations, do not promote detectable higher-order assembly, and exhibit only weak, condition-dependent interactions that are not associated with functional activation. While very large or highly concentrated nucleic acid species can produce small, context-dependent signals in selected assay configurations, these effects are minor relative to NMN and are not consistent with a defined mechanism of direct activation. Thus, under the conditions tested, nucleic acids do not function as physiologically relevant, direct activators of SARM1.

dsDNA-Induced Metabolic Stress in HEK293T Cells Is PARP1/2-Dependent and Independent of SARM1 Activation. Given the absence of reproducible dsDNA-dependent activation in vitro, we next tested whether dsDNA activates SARM1 in cells. To assess whether dsDNA-induced loss of viability depends on SARM1 in the cellular paradigm used by Wang et al. (33), we examined HEK293T cells lacking endogenous SARM1 and reconstituted with full-length SARM1 (SARM1) or an N-terminal deletion mutant lacking the mitochondrial localization sequence (ΔN-SARM1). Transfection with dsDNA reduced viability to a similar extent across all genotypes, with no significant difference between engineered SARM1 knockout HEK cells and HEK cells expressing either SARM1 or ΔN-SARM1 (Fig. 3*A*). Similar results were obtained with three distinct dsDNA substrates differing in length, indicating that dsDNA-induced loss of viability does not require SARM1 expression under these conditions. To confirm that the reconstituted constructs were functional, we treated the same cells with the cell-permeable SARM1 activators CZ-48 and G10 (8, 38). Both full-length SARM1 and ΔN-SARM1 conferred marked CZ-48 and G10 sensitivity, whereas SARM1-deficient cells remained resistant, indicating that both constructs were expressed at functionally relevant levels and retained responsiveness to pharmacologic activation (Fig. 3*A*). Because oxaliplatin was also reported to trigger SARM1-dependent death (33), we next examined oxaliplatin-induced toxicity in the same system. Again, viability was comparably reduced in SARM1 knockout cells and in cells expressing SARM1, indicating that oxaliplatin-induced death likewise occurs independently of SARM1 (Fig. 3*A*).

In an independent laboratory, we next asked whether dsDNA-induced NAD^+ depletion in WT HEK cells is accompanied by the characteristic metabolic signature of SARM1 activation. SARM1 activation results in cleavage of NAD^+ and generation of products including ADPR and cyclic ADPR (cADPR), the latter serving as a sensitive marker of SARM1 catalytic activity (35). As a positive control, vacor treatment of WT HEK293T cells expressing GFP produced the expected decrease in NAD^+ together with robust cADPR accumulation, consistent with activation of endogenous SARM1 (Fig. 3 *B* and *C*). In contrast, transfection with 90-bp dsDNA caused a similar reduction in NAD^+ in both GFP- and WT SARM1-overexpressing cells but did not produce a detectable increase in cADPR under either condition (Fig. 3 *B* and *C*). Thus, although dsDNA and vacor each reduce cellular NAD^+, only vacor generates the canonical metabolite signature of SARM1 catalytic activation, and increasing SARM1 expression does not augment the dsDNA-induced NAD^+ depletion. Because PARP1 and PARP2 (PARP1/2) are major NAD^+-consuming enzymes activated by DNA damage, we next tested whether dsDNA-induced NAD^+ loss is mediated by PARPs, rather than SARM1. SARM1 inhibition did not prevent dsDNA-induced NAD^+ depletion, whereas PARP1/2 inhibition restored NAD^+ levels toward baseline without detectable cADPR accumulation (Fig. 3 *B* and *C*).

We next examined whether this metabolic protection translated into improved cellular survival. Pharmacologic inhibition of SARM1 did not prevent dsDNA-induced loss of viability in either GFP- or SARM1-expressing cells, whereas inhibition of PARP1/2 significantly improved survival under both conditions (Fig. 3 *D* and *E*). Combined SARM1 and PARP1/2 inhibition also did not confer a statistically significant additional benefit compared with PARP1/2 inhibition alone. Together, these findings indicate that dsDNA-induced metabolic stress in HEK cells is driven by PARP-dependent NAD^+ depletion and occurs without detectable SARM1 catalytic activation. To confirm that these findings were not due to ineffective pharmacologic inhibition of SARM1, we examined vacor-induced metabolic stress in the same HEK system. In contrast to dsDNA treatment, vacor reduced viability only in cells overexpressing WT SARM1 and had no effect in GFP-control (Fig. 3 *D* and *E*). Slight differences in residual NAD^+ across

Downloaded from https://www.pnas.org by 151.76.23.94 on September 13, 2026 from IP address 151.76.23.94.

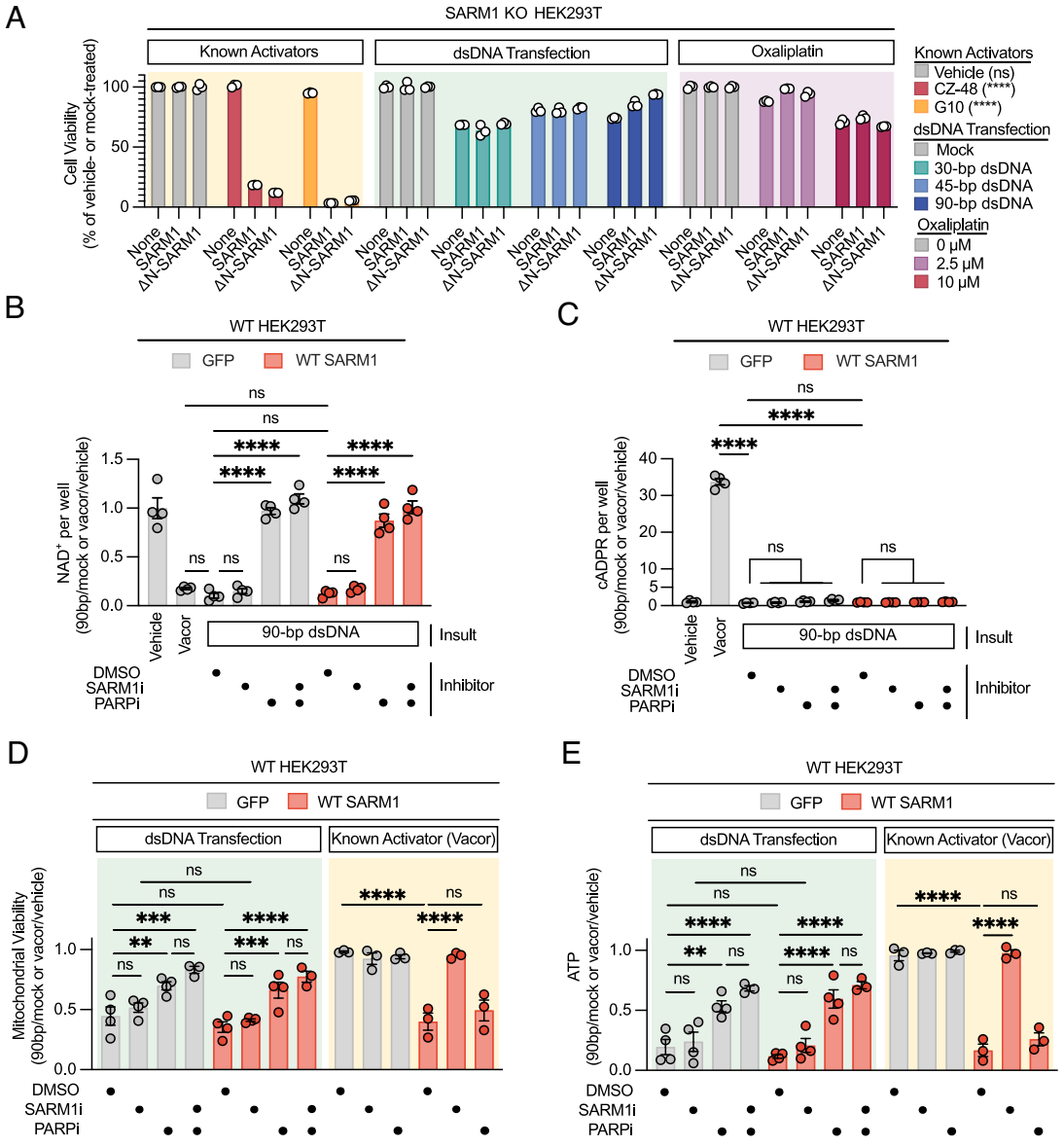

Fig. 3. dsDNA reduces NAD^+ and decreases viability in HEK cells through a PARP-dependent, SARM1-independent mechanism. (*A*) SARM1-knockout HEK293T cells expressing full-length human SARM1 (SARM1), N-terminally truncated human SARM1 lacking the mitochondrial targeting sequence (ΔN-SARM1), or no SARM1 (None) were challenged with known activators of SARM1 (yellow background), dsDNA (green background), and oxaliplatin (purple background). The same cell lines were used across the three independent experiments. Cell viability was measured 12 h after treatment with CZ-48 (200 μM) or G10 (10 μM). Both SARM1 and ΔN-SARM1 conferred marked CZ-48 and G10 sensitivity, whereas SARM1-deficient cells remained resistant. For dsDNA transfection, cells were transfected every 16 h with dsDNA (30-, 45-, or 90-bp; 2 μg/mL), and cell viability was measured 48 h after the first transfection. For oxaliplatin, cell viability was measured 60 h after exposure (n = 3 biological replicates). (*B* and *C*) Wild-type (WT) HEK293T cells expressing GFP or WT SARM1 were treated with vacor (25 μM) or transfected with 90-bp dsDNA as described in *Materials and Methods*. At 3 h after vacor treatment or 5 h after dsDNA transfection, cells were harvested for targeted LC–MS/MS quantification of NAD^+ (*B*) and cADPR (*C*). Values were normalized within plate to vehicle-treated wells for vacor or mock-transfected wells for dsDNA, separately for each genotype and inhibitor condition (n = 4 biological replicates). (*D* and *E*) WT HEK293T cells expressing GFP and WT SARM1 were treated with vacor and 90-bp dsDNA as in (*B* and *C*), and mitochondrial viability (MTT; *D*) and ATP content (CellTiter-Glo; *E*) were measured 24 h (vacor, yellow background) or 48 h (90-bp dsDNA, green background) after transfection. NB-7 (SARM1i) fully prevented vacor-induced loss of viability and ATP in WT SARM1-expressing cells, whereas ABT-888 (PARPi) had no protective effect (n = 3 to 4 biological replicates). Data in (*A*–*E*) are mean ± SEM. Statistical analysis was performed using a two-way ANOVA with Tukey's multiple comparisons test. *P < 0.05; **P < 0.01; ***P < 0.001; ****P < 0.0001; n.s., not significant.

conditions may lead to major differences in ATP and mitochondrial viability because proliferating cells can maintain ATP and mitochondrial membrane potential until there is >95% NAD^+ loss (39). This effect was fully abrogated by SARM1 inhibition but unaffected by PARP1/2 inhibition, demonstrating that SARM1 inhibition is effective in this assay configuration and that PARP1/2 inhibition does not nonspecifically rescue NAD^+-linked stress (Fig. 3 *D* and *E*). These controls confirm that the absence of protection after dsDNA treatment does not reflect ineffective SARM1 inhibition.

The 3KE Mutant Is Nonfunctional in Canonical SARM1 Paradigms in Primary Neurons. A central piece of evidence supporting the dsDNA activation model is the claim that TIR domain mutations can selectively disrupt dsDNA-dependent activation while preserving canonical NMN-dependent activation. Wang et al. (33) reported that the SARM1 TIR domain triple mutant K602E/K628E/K636E (3KE) separates these functions and retains responsiveness to its canonical allosteric activation (33). Because this claim underlies the proposed role of dsDNA binding in cellular systems and in vivo, including the use of a 3KE knock-in

Downloaded from https://www.pnas.org by 151.76.23.94 on September 13, 2026 from IP address 151.76.23.94.

mouse model (33), we directly tested whether the 3KE mutant retains canonical SARM1 function in neurons. To do so, we expressed WT SARM1 or 3KE in Sarm1-knockout primary dorsal root ganglion (DRG) neurons using lentiviral delivery (Fig. 4 *A* and *B*). Quantification of Venus fluorescence, generated from the same lentiviral transcript through the P2A-T2A cleavage cassette, as well as SARM1 protein expression by Western blot, confirmed that 3KE was expressed at similar or elevated levels compared to WT SARM1 across experiments (*SI Appendix*, Fig. S5), excluding reduced expression as an explanation for loss of function.

We next examined two paradigms, axotomy and vacor treatment, that engage SARM1 through the established NMN/NAD^+ allosteric mechanism. Axotomy engages SARM1 through injury-induced loss of NMNAT2, leading to a rise in the NMN/NAD^+ ratio, while vacor engages SARM1 through the binding of its metabolite VMN, an NMN mimetic that interacts with the SARM1 allosteric site (10). In Sarm1-knockout DRG neurons, WT SARM1 restored both axotomy- and vacor-induced degeneration, whereas 3KE-expressing neurons were indistinguishable from SARM1-deficient control neurons (Fig. 4 *C–F*). To test whether 3KE interferes with endogenous SARM1 function, we expressed 3KE in WT DRG neurons. Expression of 3KE delayed axotomy-induced degeneration, indicating that the mutant interferes with endogenous SARM1 in a dominant-negative manner (Fig. 4 *G–H*). This dominant-negative effect demonstrates that 3KE is expressed at biologically active levels and engages endogenous SARM1 in neurons. To assay SARM1 enzymatic activity, we used the fluorescent probe 1A, which reports SARM1-dependent base-exchange activity (40). Vacor treatment induced a significant increase in 1A fluorescence in WT SARM1-expressing cells, whereas 3KE-expressing cells failed to generate a catalytic signal and showed reduced fluorescence relative to control cells (Fig. 4 *I* and *J*), consistent with 3KE functioning as a dominant-negative allele.

Across two independent and well-established SARM1-dependent paradigms, the inability of 3KE to restore degeneration indicates that this mutant is nonfunctional for canonical SARM1 activity in neurons. The three lysine residues substituted in 3KE are highly conserved across TIR domains, and comparable expression levels of WT and 3KE constructs indicate that the loss of function reflects impaired catalytic activity and/or TIR-dependent assembly rather than altered protein abundance. Importantly, because 3KE is nonfunctional across all assays and conditions tested, it cannot be used to infer selective disruption of dsDNA-dependent activation.

Discussion

A recent report proposed that cytosolic dsDNA directly activates SARM1 through TIR domain binding, defining a mechanism independent of the established NMN/NAD^+-dependent pathway (33). The data presented here do not support this model. Across biochemical, cellular, and neuronal systems, we find no evidence for direct or physiologically relevant activation of SARM1 by dsDNA. In purified systems, nucleic acids do not stimulate SARM1 enzymatic activity or promote higher-order assembly under conditions in which canonical activation is robustly detected. While weak effects can be observed under selected conditions, these signals depend strongly on nucleic acid preparation and purity and do not exhibit the magnitude, consistency, or reproducibility characteristic of NMN-driven activation. These features are not consistent with a defined ligand-mediated activation mechanism and instead are most consistent with nonspecific or assay-dependent effects.

In cellular systems, dsDNA transfection induces NAD^+ depletion and metabolic stress, but this response occurs independently of SARM1 and is instead mediated by PARP-dependent NAD^+ consumption. The absence of SARM1-dependent biochemical signatures, including cADPR production, together with the lack of SARM1-dependent functional effects, indicates that dsDNA does not engage SARM1 in HEK293T cells under the conditions tested. PARP activation can trigger secondary SARM1 activation upon DNA damage in neurons (41). The absence of this effect in HEK293T cells may reflect differences in the kinetics of NAD^+ loss upon dsDNA-induced PARP activation, NAD^+ compartmentalization, and/or NAD^+ resynthesis between HEK293T and neurons. These findings indicate that NAD^+ depletion alone is not sufficient to infer SARM1 activation in cellular systems where multiple NAD^+-consuming pathways are engaged. Evidence for the physiological relevance of dsDNA-stimulated SARM1 activation in Wang et al. (33) relies on the use of the SARM1 TIR domain mutant 3KE, which was proposed to selectively disrupt DNA-mediated activation while preserving canonical function. Our findings demonstrate that 3KE does not retain canonical SARM1 activity and instead behaves as a loss-of-function allele. Therefore, it cannot be used to distinguish between activation mechanisms or support a separation-of-function model.

SARM1 has emerged as a central driver of axon degeneration in diverse neurodegenerative settings, and small-molecule inhibitors are under clinical evaluation (42). Accurate definition of the mechanisms that activate SARM1 is therefore essential for therapeutic development and mechanistic interpretation of disease models. Our findings reinforce the view that SARM1 activation is governed by metabolic imbalance, and while additional regulatory mechanisms of SARM1 activation exist (19, 43–45), the data presented here do not support a model in which SARM1 acts as a direct dsDNA sensor. Clarifying the molecular basis of SARM1 engagement is essential for understanding how diverse forms of injury and disease converge on axonal degeneration pathways.

Materials and Methods

HEK293T Cell Lines. HEK293T (ATCC) and HEK-293T SARM1$^{-/-}$ cells [Zhang et al., (20)] were maintained at 37 °C in a humidified incubator with 5% or 8% CO_2. Cells were cultured in Dulbecco's Modified Eagle Medium (Gibco) supplemented with 10% fetal bovine serum or a 1:1 mixture of Freestyle 293 Expression Medium (Gibco) and Ex-Cell 293 Medium (Sigma). HEK293T cultures were additionally supplemented with L-glutamine and penicillin–streptomycin. Cells were passaged every 3 to 4 d.

Expression systems included GFP, full-length WT human SARM1 (SARM1), full-length K602E/K628E/K636E human SARM1 (3KE SARM1), and N-terminally truncated SARM1 (ΔN-SARM1; residues 28 to 724). Stable lines were generated via lentiviral transduction followed by fluorescence-based enrichment or puromycin selection.

Primary Neuron Culture. Dorsal root ganglion (DRG) spot cultures were prepared as described previously (46). DRGs were dissected from embryonic day 13.5 WT CD1 mice and Sarm1$^{-/-}$ mice, dissociated in 0.05% trypsin (Gibco) at 37 °C, and triturated in plating medium.

Dissociated neurons were seeded as spot cultures into 96-well plates precoated with 0.1 mg/mL poly-D-lysine and 0.1 mg/mL laminin. Neurons were maintained in Neurobasal medium supplemented with 2% B27, 50 ng/mL nerve growth factor, and 10 μM 5-fluoro-2′-deoxyuridine. Lentivirus was added at DIV1, and experiments were performed at DIV6–8 following media replacement at DIV5–6.

Recombinant Protein Systems. Human SARM1 constructs, including full-length SARM1 (residues 1 to 724), ΔN-SARM1 (residues 28 to 724), and SARM1^{TIR} constructs (residues 561 to 700 or 561 to 724), were expressed in mammalian or

Downloaded from https://www.pnas.org by 151.76.23.94 on September 13, 2026 from IP address 151.76.23.94.

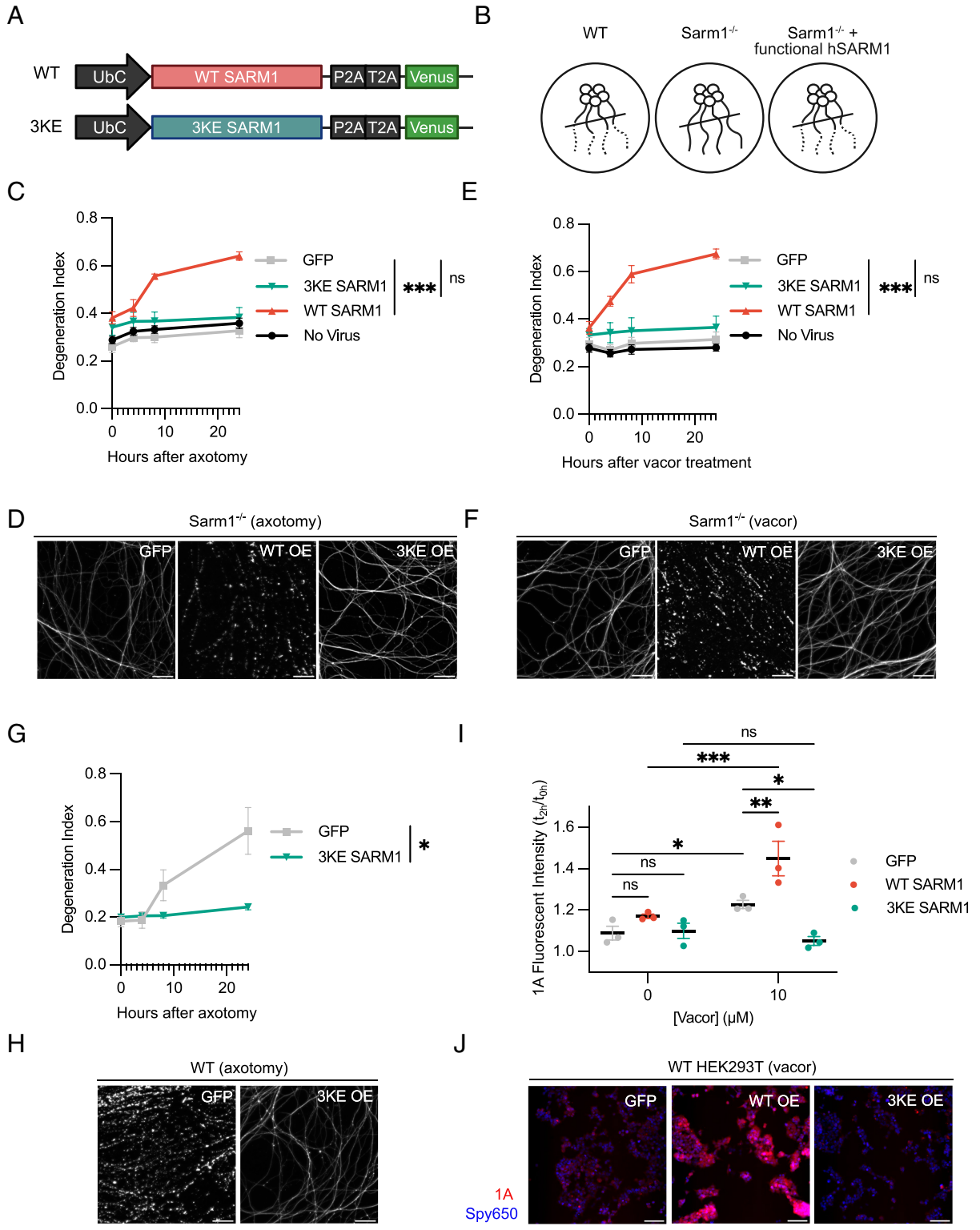

Fig. 4. The 3KE mutation disrupts SARM1 activation by axotomy and vacor. (*A*) Schematic diagram of fluorescent lentiviral constructs expressing WT human SARM1 (WT SARM1), or human SARM1 possessing the K602E/K628E/K636E mutation (3KE SARM1). (*B*) Experimental design illustrating rescue paradigm in DRG neurons. (*C* and *D*) Sarm1$^{-/-}$ DRG spot cultures were transduced with lentivirus and subjected to axotomy. Axon degeneration was quantified over time as degeneration index (DI) from brightfield images as described in *Materials and Methods* (*C*). Representative βIII-tubulin (TUJ1) immunofluorescence images at 24 h postaxotomy (*D*) ($n = 4$ biological replicates, each with ≥3 technical replicates). (Scale bar, 100 μm.) (*E* and *F*) Sarm1$^{-/-}$ DRG spot cultures were transduced as in (*C*) and treated with vacor (50 μM). DI time course (*E*) and representative TUJ1 images at 24 h (*F*) ($n = 4$ biological replicates, each with ≥3 technical replicates). (Scale bar, 100 μm.) (*G* and *H*) WT DRG spot cultures were transduced as in (*C*) to test dominant negative effects of 3KE expression and subjected to axotomy. DI time course (*G*) and representative TUJ1 images at 24 h (*H*) ($n = 4$ biological replicates, each with ≥3 technical replicates). (Scale bar, 100 μm.) (*I* and *J*) HEK293T cells stably expressing lentiviral constructs were loaded with the fluorescent SARM1 activity probe 1A and Spy650 nuclear dye, then treated with vacor (10 μM). Conditions: control vector (GFP, gray), WT SARM1 overexpression (WT SARM1, red), or 3KE SARM1 overexpression (3KE SARM1; green). 1A fluorescence, reporting direct SARM1 catalytic base-exchange activity, was quantified at 0 and 2 h (*I*), with representative composite images shown for the vacor-treated condition at 2 h (*J*) ($n = 3$ biological replicates, each with 3 technical replicates). (Scale bar, 100 μm.) Data in (*C*, *E*, *G*, and *I*) are mean ± SEM. Two-way ANOVA with Dunnett's multiple comparison test was used to compare indicated groups. Significance annotations indicate comparisons at 24 h for DRG assays and 2 h for HEK293T assays. *$P < 0.05$; **$P < 0.01$; ***$P < 0.001$; ****$P < 0.0001$; n.s., not significant.

Downloaded from https://www.pnas.org by 151.76.23.94 on September 13, 2026 from IP address 151.76.23.94.

bacterial systems depending on the application. Constructs contained N-terminal affinity tags (Flag, Strep, or His_6), with or without TEV-protease cleavage sites.

SARM1 and ΔN-SARM1 were expressed in HEK293T or Expi293F cells as previously described (12, 13, 17, 20). Cells were lysed in HEPES-based lysis buffer supplemented with protease inhibitors and in some cases, digitonin or TCEP. Lysates were clarified by centrifugation and subjected to affinity purification (anti-Flag, Strep-Tactin, or HisTrap), followed by elution with Flag peptide, desthiobiotin, or imidazole, respectively. Eluted proteins were used directly or digested with TEV protease and further purified by size-exclusion chromatography.

$SARM1^{TIR}$ constructs were expressed in *Escherichia coli* BL21(DE3) cells, and protein was purified by immobilized metal affinity chromatography as described previously (4, 20, 47). In some cases, protein was further purified following tag cleavage by size-exclusion chromatography.

Peak fractions were analyzed by SDS–PAGE, and proteins were either used immediately or stored at −80 °C. Biochemical assays were performed using independently prepared protein batches as described.

Generation of Plasmids. Full-length WT SARM1 was cloned into the pWPI vector with an N-terminal Flag tag, as described previously (20), and the FCIV vector with C-terminal tandem T2A/P2A self-cleaving peptide sequences followed by Venus, as described previously (12). The 3KE mutant construct was generated via PCR-based mutagenesis with primers containing K602E, K628E, and K636E, followed by insertion between *Bam*HI and *Bst*XI sites on the FCIV SARM1 construct. ΔN-SARM1 was cloned into several vectors: 1) pLVX-IRES-ZsGreen with C-terminus TEV-protease cleavage site, FLAG, and His_6 tags by cloning between *Eco*RI and *Bam*HI sites, as described previously (10); 2) PSF-CMV-AMP with N-terminus TEV-protease cleavage site, His_6 tag, and AVI-tags as described previously (12); 3) pLenti-puro vector (#17452, Addgene) with N-terminal Strep and Flag tags using the Gateway™ system (Thermo Fisher). Last, $SARM1^{TIR}$ was cloned into the following vectors: 1) pMCSG7 with N-terminal His_6-tag and TEV-protease cleavage site (4); 2) pWPI as described previously (20).

Generation and Acquisition of dsDNA Substrates. Lyophilized sense and antisense oligonucleotides of varying lengths (30-bp, 45-bp, 54-bp, 81-bp, and 90-bp) were purchased from Sigma Genosys or IDT, resuspended in nuclease-free water, and annealed in buffer containing 60 to 100 mM NaCl, by heating to 95 °C followed by gradual cooling. Synthetic dsDNA substrates were evaluated in parallel with PCR-amplified and plasmid-derived DNA as described below.

For PCR-derived dsDNA, a 125-bp fragment was amplified and purified using a DNA Gel Extraction Kit (Omega Bio-tek, #D2500). The corresponding sequence was also generated by chemical synthesis and HPLC purification (Hechengyuan, Shenzhen, China). Where indicated, dsDNA samples were further purified by sodium acetate–ethanol precipitation (0.3 M sodium acetate, two volumes ethanol, −20 °C incubation), followed by washing and resuspension in nuclease-free water.

Plasmid-based DNA substrates included pUC19, poly(dG:dC), poly(dA:dT), and the 10,853-bp pLVX-SARM1-IRES-Green construct.

The MST DNA probe (5′-128 bp-Cy5-3′) was synthesized using PCR. A forward primer (5′-TAATACGACTCACTATAGGG) and a reverse primer (5′-CCAGATCTACACCAGAAGA) containing the Cy5 fluorescent tag were used to amplify from the T7 promoter in the pMCSG7 plasmid for 128-bp.

All DNA substrates were handled under nuclease-free conditions and diluted in the indicated buffers prior to use.

NMR-Based Enzymatic Assay. Human ΔN-SARM1 NMR samples were prepared in 175 μL of HBS buffer (50 mM HEPES, 150 mM NaCl, 1 mM $MgCl_2$, pH 7.5 in H_2O) with 20 μL D_2O and 5 μL DMSO-d_6, yielding a final volume of 200 μL. $SARM1^{TIR}$ NMR samples were prepared in the same manner but without DMSO-d_6, in 175 μL of HBS buffer and 25 μL D_2O to a final volume of 200 μL. Each sample was subsequently transferred to a 3 mm Bruker NMR tube. All ^1H NMR spectra were acquired with either a Bruker Avance Neo 600 MHz NMR spectrometer equipped with a QCI-F cryoprobe at 298 K, or a Bruker Neo 900 MHz NMR spectrometer equipped with a cryogenically cooled probe. For the Bruker Avance Neo 600 MHz NMR instrument H_2O resonance suppression was achieved using the P3919GP water-suppression pulse program (3-9-19 pulse sequence with gradients) (48), with an acquisition delay of 2 s and 32 scans per sample. For the Bruker Neo 900 MHz NMR instrument H_2O resonance suppression was achieved using excitation sculpting (180° water-selective) and pulsed field gradients (Bruker zgesgp). For each reaction, spectra were recorded at multiple time points, including 10 min, 2 h, 4 h, 8 h, and 16 h, depending on instrument availability. All spectra were processed by TopSpin™ (Bruker) and MNova (Mestrelab Research). The reaction progression was calculated based on the integration of nonoverlapping resonance peaks, which vary depending on sample composition, from pairs of substrates and products, such as NAD^+ and nicotinamide, respectively. The detection limit (signal-to-noise ratio >2) was estimated to be 10 μM.

LC-MS/MS-Based Enzymatic Assay. LC–MS/MS analysis of NADase reaction products was performed as described previously (20, 38). Reactions were carried out in 50 μL volumes containing 0.1 μM full-length SARM1 and 2 mM NAD^+ in reaction buffer (20 mM Tris-HCl, pH 7.5, 100 mM NaCl, 1 mM $MgCl_2$), with dsDNA substrates or NMN (1 mM) as a positive control.

After incubation, reactions were quenched with acetonitrile and analyzed by UHPLC for NAD^+, ADPR, cADPR, and nicotinamide.

SARM1 activity was quantified as NAD^+ consumption and/or accumulation of reaction products relative to enzyme-only controls under identical conditions.

HPLC-Based Enzymatic Assay. Reaction mixtures (typically 100 μL final) contained pure ΔN-SARM1 at 10 to 12 μg/mL (e.g., ~140 nM of monomer), 100 mM NaCl, and 1 mM $MgCl_2$ in 50 mM HEPES buffer, pH 7.5. Double-stranded DNA was included at 0.05 μM (10,853-bp circular dsDNA) and 0.2 μM (54- or 81-bp linear dsDNA) final concentration, followed by preincubation for 20 min, then 2 mM NAD^+ was added to start the reactions. Temperature control was set at 25 °C and aliquots of each assay mixture were collected at 0 min, 30 min, and 60 min, treated with perchloric acid and analyzed by C18-HPLC as described (5). NMN (0.5 mM) was used in place of dsDNA as positive control, while negative controls were represented by blank mixtures without enzyme, treated and analyzed in parallel.

Reaction products (ADPR and cADPR) were quantified and summed, and reaction rates were calculated as NAD^+ consumption equivalents relative to enzyme-only controls as previously reported (5). Initial rates of SARM1 activity (nmol/min/mg) were measured in triplicate for each condition tested. Values were then converted to relative activation fold vs. the control without dsDNA.

Fluorometric PC6 Enzymatic Assay. SARM1 NADase activity was measured using the fluorogenic probe PC6, synthesized as described previously (36). Assays were performed with purified protein (SARM1 or ΔN-SARM1) or clarified cell lysates (ΔN-SARM1). Reactions contained SARM1, PC6 (10 or 50 μM), and NAD^+ (100 μM or 2 mM) in reaction buffer (DPBS or PBS). For activation assays, NMN or dsDNA was added at reaction initiation.

Fluorescence was recorded kinetically at excitation 390 nm and emission 510 to 520 nm. Initial reaction rates (RFU min^{-1}) were calculated from the linear portion of the fluorescence time course and used as a measure of SARM1 NADase activity.

EMSA. 0.1 μM 5′-Cy5-labeled dsDNA was incubated with SARM1 protein in buffer (20 mM HEPES pH 7.5, 150 mM NaCl, 10 mM $MgCl_2$) at 37 °C for 30 min. Samples were resolved on agarose gels under electrophoretic conditions optimized to preserve higher-order protein–DNA complexes.

Mass Photometry. Mass photometry data were collected on a Refeyn OneMP system (Refeyn Ltd, Oxford, UK). High precision glass coverslips (Marienfeld Ltd) were thoroughly washed three times using Milli-Q® H_2O, ethanol and 2-propanol, followed by drying under a stream of nitrogen gas. For sample loading, a silicon gasket (Refeyn Ltd) was placed on the slide. To focus the objective, 16 μL of buffer (10 mM HEPES pH 7.5, 150 mM NaCl) was placed in a well. Thereafter, 4 μL of the test sample was loaded and mixed by pipetting the volume up–down five times, followed by immediate measurement. Mass photometry data were acquired and analyzed using AcquireMP and DiscoverMP software (Refeyn Ltd), respectively. A Gaussian curve was fitted to the resulting peaks in the contrast histogram (depicting the number of detected molecules and their corresponding contrast value), where each peak represented a subpopulation of molecules with a particular molecular weight (MW). The contrast values of observed counts were converted into MW by calibration using a control protein of known MW and size; in-house bovine serum albumin (BSA), with a monomer at 66 kDa, a dimer at 132 kDa, and a trimer at 198 kDa. For measuring dsDNA molecular weight, the glass coverslip was first coated with Poly-L-Lysine (PLL) before the dsDNA sample

Downloaded from https://www.pnas.org by 151.76.23.94 on September 13, 2026 from IP address 151.76.23.94.

was loaded. The contrast values of observed counts were converted into MW by calibration using a commercial DNA ladder (Invitrogen™ Low DNA Mass Ladder, ThermoFisher Scientific).

Analytical Size-Exclusion Chromatography. After incubation, 500 μL of each sample was loaded onto a S200 10/300 column (Cytiva) using an Akta Pure device (Cytiva) at 0.5 mL/min. Analysis of chromatograms and image preparation was performed in Unicorn 7 software (Cytiva) and Excel (Microsoft). Peak fractions were analyzed by SDS-PAGE.

Microscale Thermophoresis. Generation of the Cy5-labeled DNA probe is described above. $SARM1^{TIR}$ was serially diluted in a 2:1 ratio across 16 points, with the highest concentration being 170 μM in gel filtration buffer (10 mM HEPES, 150 mM NaCl, 1 mM DTT, pH 7.5). Each point had a final volume of 15 μL, and 5 μL of the Cy5-labeled fragment was added with the final dsDNA concentration of 10 nM. Samples were left on ice for 20 min and centrifuged and equilibrated to room temperature and transferred into Monolith Nt.115 capillaries (NanoTemper Technologies). Capillaries were loaded onto a Monolith NT.115 at ambient temperature of 22 °C. Scans were recorded using 65% LED power and medium MST power. MO.Affinity analysis software was used to fit a Hill model, with the cold time set to −1.5 to −0.5 s and hot time to 0.5 to 1.5 s.

Cryo-EM Sample Preparation and Screening. SARM1 (31 μM) or $SARM1^{TIR}$ (47 μM) were incubated with 90-bp dsDNA (5 μM) or 300-bp dsDNA (1.5 μM) on ice for 60 min. A 3 μL aliquot of each sample was applied to Quantifoil R1.2/1.3 300-mesh Au holey carbon grids, blotted, and plunge-frozen in liquid ethane using an FEI Vitrobot. Grids were screened on a 200 kV Titan Arctica microscope equipped with a Gatan K2 Summit direct electron detector. Images were acquired in super-resolution mode using SerialEM (49) at a magnification of 36,000×, corresponding to a physical pixel size of 1.157 Å. Each micrograph was recorded as 40 frames over a total exposure time of 8 s, with an electron dose rate of 8 $e^{-}pixel^{-1}\,s^{-1}$, resulting in a total accumulated dose of 47.8 $e^{-}\,Å^{-2}$. Micrographs were collected at a defocus of 2.5 μm.

Negative-Stain EM. 4 μL of sample was placed on a carbon-coated copper grid and incubated for 60 s. The grid was then washed with Milli-Q® H_2O and stained with 1% uranyl acetate for 60 s and air-dried. The images were collected on a JEOL JEM-1400Flash TEM transmission electron microscope at 20,000 to 60,000× magnification at 80 keV.

Lentivirus Production. Lentivirus was produced in HEK293T cells by transient transfection of the transfer plasmid together with psPAX2 and VSV-G or pMD2.G (Addgene #12259) using FuGENE 6 transfection reagent [Promega (Madison, WI); Cat.#E2691]. Viral supernatants were harvested at 48 h posttransfection, clarified by centrifugation (500×*g*, 10 min, 4 °C), and concentrated using Lenti-X-Concentrator.

Transfection of dsDNA in Cells. For WT SARM1 experiments, dsDNA was transfected using Lipofectamine 3000 according to the manufacturer's protocol. 90-bp dsDNA was transfected at 0.05 μg per well (96-well format) or 0.25 μg per well (24-well format). Mock transfections were performed using the annealing buffer diluted in Opti-MEM and processed in the same way.

For SARM1 KO experiments, cells were seeded in 12-well plates and transfected every 16 h with 2 μg/mL 30-bp, 45-bp, or 90-bp dsDNA fragments using Lipofectamine 2000 (Thermo Fisher Scientific) or Lipomaster 3000 (Vazyme) according to the manufacturer's instructions. Cell viability was assessed 48 h posttransfection using the CellCounting-Lite Cell Viability Assay. For oxaliplatin treatment, cells were exposed to 5 μM or 10 μM oxaliplatin for 60 h, after which viability was measured using the same assay and normalized to the untreated control for each cell line.

MTT Assay. HEK293T cells were seeded at 55,000 cells/cm^2 in 96-well plates. The next day, medium was replaced with complete DMEM containing inhibitors or vehicle control for 4 to 6 h: SARM1 inhibitor NB-7 (50 μM) and/or PARP inhibitor ABT-888 (12.5 μM). Vacor was then added as a 2× solution to achieve 25 μM final concentration, or cells were transfected with 90-bp dsDNA as described above. After 24 (vacor) or 48 (90-bp dsDNA) h, the MTT reagent was added (10 μL per well) and incubated for 4 to 6 h at 37 °C. Crystals were solubilized with isopropanol (100 μL per well), and absorbance was measured at 570 nm with background subtraction at 690 nm using a plate reader.

Relative viability was calculated per genotype and drug condition by normalizing vacor-treated wells to vehicle-treated wells, or dsDNA-transfected wells to mock-transfected wells within the same plate.

ATP Assay. ATP assays were performed in WT and SARM1 knockout (KO) HEK293T cells.

In WT SARM1 experiments, cells were seeded and treated identically to the MTT assay. Cellular ATP content was measured using CellTiter-Glo (Promega) according to the manufacturer's instructions. Briefly, reagent and plates were equilibrated to room temperature for 15 to 30 min. CellTiter-Glo was added 1:1 to culture volume (100 μL per well), plates were shaken for 2 to 3 min to induce lysis, incubated for an additional 10 min at room temperature, and luminescence was measured on a plate reader. Relative ATP signal was normalized within plate as described for MTT.

In SARM1 KO experiments, HEK293T cells expressing SARM1, DN-SARM1, or no SARM1 were maintained under standard culture conditions. For dsDNA transfection, cells were seeded in 12-well plates and transfected every 16 h with 2 μg/mL 30-bp, 45-bp, or 90-bp dsDNA fragments using Lipofectamine 2000 (Thermo Fisher Scientific) or Lipomaster 3000 (Vazyme) according to the manufacturer's instructions. Cell viability was assessed 48 h posttransfection using the CellCounting-Lite Cell Viability Assay. For oxaliplatin treatment, cells were exposed to 5 μM or 10 μM oxaliplatin for 60 h, after which viability was measured using the same assay and normalized to the untreated control for each cell line.

Metabolite Extraction and Measurement by LC–MS/MS. HEK293T cells were seeded at 55,000 cells/cm^2 in 24-well plates. Drug treatments and/or dsDNA transfections were performed as described above. Metabolites were extracted at 6 h posttransfection. Cells were washed with ice-cold 0.9% NaCl, and metabolites were extracted with ice-cold 50% methanol (MeOH) (160 μL per well) for 5 min. Chloroform (40 μL per well) was added to the solution, the solution was mixed well, and it was then centrifuged (15,000×*g*, 10 min, 4 °C). The upper aqueous phase was collected for LC–MS/MS. Extracts were dried in a SpeedVac and stored at −80 °C until metabolite measurement.

Lyophilized samples were resuspended in 5 mM ammonium formate and clarified by centrifugation (13,000×*g*, 10 min, 4 °C). NMN, NAD^+, and cADPR were quantified by LC–MS/MS as described previously (41). Briefly, targeted LC–MS/MS was carried out on an Agilent 1290 Infinity II LC system coupled to an Agilent 6470 triple-quadrupole mass spectrometer. Chromatographic separation was performed on an Atlantis T3 reversed-phase column (2.1 × 150 mm, 3 μm; Waters) with a matching VanGuard guard cartridge (2.1 × 5 mm, 3 μm; Waters). The mobile phases were 5 mM ammonium formate in water (A) and methanol (B), delivered at 0.15 mL per min. Samples (10 μL) were injected after equilibration at 0% B, which was maintained for 2 min, followed by a programmed gradient: 0 to 20% B over 4 min, 20 to 50% B over 2 min, hold at 50% B for 2 min, then return to 0% B over 5 min and re-equilibrate for 9 min (24 min total).

The mass spectrometer was operated with an electrospray source in positive-ion MRM mode. The monitored precursor/product ion pairs were NAD^+ (m/z 664→428), NMN (m/z 335→123), cADPR (m/z 542→428), and ATP (m/z 508→136). Instrument parameters (including fragmentor, collision energy, and cell accelerator voltage) were tuned individually for each transition. Data collection and quantification were performed in MassHunter Workstation (vB.08.00, Agilent) using the external standard curves, and analyte signals were normalized to total protein.

Axon Degeneration Assay. DRG spot cultures in a 96-well plate were treated with 50 μM vacor or axotomized with a microblade (34). Brightfield images were acquired at 0, 4, 8, and 24 h after injury on the IN Cell Analyzer 6000 with identical acquisition settings across conditions. Axon degeneration was quantified using the ImageJ/Fiji macro ADJudge as described previously (46). For each well (technical replicate), 8 to 10 fields of view were quantified and averaged to yield a single DI value.

Immunofluorescence Staining. At 24 h after vacor or axotomy injury, DRG spot cultures were fixed in 4% paraformaldehyde for 15 min at room temperature, followed by three PBS washes. Cells were then blocked and permeabilized in 10% normal goat serum in PBS containing 0.1% Triton x-100 for 1 h at room temperature. Primary antibody incubation was performed overnight at 4 °C in

Downloaded from https://www.pnas.org by 151.76.23.94 on September 13, 2026 from IP address 151.76.23.94.

blocking buffer using rabbit anti-βIII-tubulin (TUJ1; 1:1,000). After three PBS washes, cultures were incubated for 1 h at room temperature with Alexa Fluor 568 goat anti-rabbit secondary antibody (1:1,000) and Hoechst 33342 (1:5,000) in blocking buffer. Following three PBS washes, images were acquired on the IN Cell Analyzer 6000 with uniform exposure settings across conditions.

1A Probe Imaging. The 1A probe was synthesized as described in Huang et al. (40). HEK293T cells were seeded at 55,000 cells/cm^2 in 96-well plates. The next day, medium was replaced with complete DMEM containing 1A probe (10 μM final) and Spy650 (1:1,000 dilution). After 2 h incubation at 37 °C, baseline images (0 h timepoint) were acquired on an IN Cell Analyzer 6000. Vacor was then added as a 2× solution to achieve 10 μM final concentration. After an additional 2 h incubation, images were acquired for the 2 h timepoint.

Fluorescence channels were configured as follows: 1A probe (Ex 405 nm/Em 610 nm) and Spy650 (Ex 642 nm/Em 706 nm). Images were acquired on the IN Cell Analyzer 6000 with uniform exposure settings across conditions.

Quantification and Statistical Analysis. For purified protein experiments, biological replicates represent independent protein preparations. For primary neuron experiments, biological replicates represent independent embryo dissections. For HEK293T experiments, biological replicates represent independent passages. All data are represented as mean ± SEM; $*P < 0.05$, $**P < 0.01$, $***P < 0.001$, $****P < 0.0001$. Exact n, statistical tests, and *P*-values are reported in figure legends. Statistical tests were performed in GraphPad Prism 10.

Data, Materials, and Software Availability. Data have been deposited in Digital Commons Data@Becker (50). All other study data are included in the article and/or *SI Appendix*.

ACKNOWLEDGMENTS. This work was supported by the NIH (Grant No. NS087632 to A.D. and J.M.; NS065053 to A.D.), the National Health and Medical Research Council (Investigator Grants 1196590 and 2042089 to T.V.; 2025931 to B.K.), the Ministry of Science and Technology of the People's Republic of China (institutional Grant to X.W.), Tsinghua University (institutional Grant to X.W.), the Beijing Municipal Commission of Science and Technology (institutional Grant to X.W.), the National Natural Science Foundation of China (Grant No. 32470755 to Y.J.Z.; 32471252 to Z.Z.), the National Facility for Structural Biology at the Fondazione Human Technopole (Call for Access 25-SB-ROUND-1, Project ID 2160736 to G.O.), and the Beijing Natural Science Foundation (Grant No. Z240013 to Z.Z.). We acknowledge the Centre for Microscopy and Microanalysis, University of Queensland and staff. We thank the Cryo-EM platform at the School of Life Sciences (SLS), Peking University, for assistance with cryo-EM data collection. We thank Xiaolu Sun, Alicia Neiner, and Kelli Simburger for support with tissue culture, molecular cloning, and metabolomics. Additional support was provided by the Center for Life Sciences, the School of Pharmaceutical Sciences at Peking University, and the Qidong-SLS Innovation Fund (to Z.Z.). Diagrams used in the manuscript were generated using BioRender.com.

Author affiliations: [a]Department of Developmental Biology, Washington University School of Medicine, St. Louis, MO 63110; [b]Department of Genetics, Washington University School of Medicine, St. Louis, MO 63110; [c]Institute for Biomedicine and Glycomics, Griffith University, Gold Coast, QLD 4222, Australia; [d]School of Chemistry and Molecular Biosciences, Institute for Molecular Bioscience and Australian Infectious Diseases Research Centre, University of Queensland, Brisbane, QLD 4072, Australia; [e]National Institute of Biological Sciences, Beijing 102206, China; [f]State Key Laboratory of Natural and Biomimetic Drugs, Department of Molecular and Cellular Pharmacology, Center for Life Sciences, Academy for Advanced Interdisciplinary Studies, School of Pharmaceutical Sciences, Peking University, Beijing 100191, China; [g]Division of Biomedical Health Sciences, School of Medicine, The Chinese University of Hong Kong, Shenzhen 518172, China; [h]Needleman Center for Neurometabolism and Axonal Therapeutics, St. Louis, MO 63110; and [i]Department of Clinical Sciences, Section of Biochemistry, Polytechnic University of Marche, Ancona 60131, Italy

Author contributions: A.H.K., B.P.M., M.S., W.Z., Q.Z., Z.Z., Y.J.Z., G.O., X.W., J.M., B.K., T.V., and A.D. designed research; A.H.K., B.P.M., M.S., W.Z., Q.Z., Y.J., V.M., P.H., W.G., J.Y.Y., and G.O. performed research; W.Z., Q.Z., A.J.B., R.D.M., Z.Z., Y.J.Z., G.O., X.W., J.M., B.K., T.V., and A.D. analyzed data; and A.J.B., R.D.M., Z.Z., Y.J.Z., G.O., X.W., J.M., B.K., T.V., and A.D. wrote, reviewed, and edited the paper.

Reviewers: C.H., Genentech Inc; and T.L.S., Harvard Medical School.

Competing interest statement: X.W. is a cofounder and consultant of Sironax, a biotech startup working on developing therapeutic agents against neurodegenerative diseases. X.W owns 5.5% of stock of Sironax Inc., a biotech start-up working on neurodegenerative diseases. Sironax has no financial or employee involvement in the current work. J.M. and A.D. are co-founders, scientific advisory board members, and shareholders of Disarm Therapeutics, a wholly owned subsidiary of Eli Lilly. B.K. is a shareholder of Disarm Therapeutics as well. J.M. and A.D. are also scientific advisory board members of Asha Therapeutics. The remaining authors declare no competing interests.

1. J. M. Osterloh *et al.*, dSarm/Sarm1 is required for activation of an injury-induced axon death pathway. *Science* **337**, 481–484 (2012).
2. J. Gerdts, E. J. Brace, Y. Sasaki, A. DiAntonio, J. Milbrandt, SARM1 activation triggers axon degeneration locally via NAD+ destruction. *Science* **348**, 453–457 (2015).
3. K. Essuman *et al.*, The SARM1 Toll/interleukin-1 receptor domain possesses intrinsic NAD+ cleavage activity that promotes pathological axonal degeneration. *Neuron* **93**, 1334–1343.e5 (2017).
4. S. Horsefield *et al.*, NAD+ cleavage activity by animal and plant TIR domains in cell death pathways. *Science* **365**, 793–799 (2019).
5. C. Angeletti *et al.*, SARM1 is a multi-functional NAD(P)ase with prominent base exchange activity, all regulated bymultiple physiologically relevant NAD metabolites. *iScience* **25**, 103812 (2022).
6. F. I. Hinz, C. C. Hoogenraad, DLK, NMNAT2, and SARM1: Judge, jury, and executioner in axon degeneration. *Annu. Rev. Biochem.* **95**, 595–624 (2026).
7. J. Gilley, G. Orsomando, I. Nascimento-Ferreira, M. P. Coleman, Absence of SARM1 rescues development and survival of NMNAT2-deficient axons. *Cell Rep.* **10**, 1974–1981 (2015).
8. Z. Y. Zhao *et al.*, A cell-permeant mimetic of NMN activates SARM1 to produce cyclic ADP-ribose and induce non-apoptotic cell death. *iScience* **15**, 452–466 (2019).
9. T. Wu *et al.*, Neurotoxins subvert the allosteric activation mechanism of SARM1 to induce neuronal loss. *Cell Rep.* **37**, 109872 (2021).
10. A. Loreto *et al.*, Neurotoxin-mediated potent activation of the axon degeneration regulator SARM1. *eLife* **10**, e72823 (2021).
11. M. Di Stefano *et al.*, A rise in NAD precursor nicotinamide mononucleotide (NMN) after injury promotes axon degeneration. *Cell Death Differ.* **22**, 731–742 (2015).
12. M. D. Figley *et al.*, SARM1 is a metabolic sensor activated by an increased NMN/NAD+ ratio to trigger axon degeneration. *Neuron* **109**, 1118–1136.e11 (2021).
13. Y. Jiang *et al.*, The NAD+-mediated self-inhibition mechanism of pro-neurodegenerative SARM1. *Nature* **588**, 658–663 (2020).
14. M. Sporny *et al.*, Structural basis for SARM1 inhibition and activation under energetic stress. *eLife* **9**, e62021 (2020).
15. Y. Shi *et al.*, Structural basis of SARM1 activation, substrate recognition, and inhibition by small molecules. *Mol. Cell* **82**, 1643–1659.e10 (2022).
16. C. Shen *et al.*, Multiple domain interfaces mediate SARM1 autoinhibition. *Proc. Natl. Acad. Sci. U.S.A.* **118**, e2023151118 (2021).
17. Y. N. Hou *et al.*, A conformation-specific nanobody targeting the nicotinamide mononucleotide-activated state of SARM1. *Nat. Commun.* **13**, 7898 (2022).
18. H. S. Loring *et al.*, A phase transition enhances the catalytic activity of SARM1, an NAD+ glycohydrolase involved in neurodegeneration. *eLife* **10**, e66694 (2021).
19. J. Shi, Y. E. Kim, N. J. DeRuiter, P. Kadav, M. Tessier-Lavigne, Caspase-3 cleaves and activates the NADase SARM1 to promote apoptosis, linking two cell death mechanisms. *Proc. Natl. Acad. Sci. U.S.A.* **123**, e2528118123 (2026).
20. W. Zhang *et al.*, SARM1 activation promotes axonal degeneration via a two-step phase transition. *Nat. Chem. Biol.* **22**, 435–445 (2026).
21. J. Gilley, M. P. Coleman, Endogenous Nmnat2 is an essential survival factor for maintenance of healthy axons. *PLoS Biol.* **8**, e1000300 (2010).
22. D. W. Summers, A. DiAntonio, J. Milbrandt, Mitochondrial dysfunction induces Sarm1-dependent cell death in sensory neurons. *J. Neurosci.* **34**, 9338–9350 (2014).
23. A. Loreto *et al.*, SARM1 activation induces reversible mitochondrial dysfunction and can be prevented in human neurons by antisense oligonucleotides. *Neurobiol. Dis.* **213**, 106986 (2025).
24. Y. Sato-Yamada *et al.*, A SARM1-mitochondrial feedback loop drives neuropathogenesis in a Charcot-Marie-Tooth disease type 2A rat model. *J. Clin. Invest.* **132**, e161566 (2022).
25. S. Geisler *et al.*, Prevention of vincristine-induced peripheral neuropathy by genetic deletion of SARM1 in mice. *Brain* **139**, 3092–3108 (2016).
26. N. Henninger *et al.*, Attenuated traumatic axonal injury and improved functional outcome after traumatic brain injury in mice lacking Sarm1. *Brain* **139**, 1094–1105 (2016).
27. K. W. Ko, J. Milbrandt, A. DiAntonio, SARM1 acts downstream of neuroinflammatory and necroptotic signaling to induce axon degeneration. *J. Cell Biol.* **219**, e201912047 (2020).
28. R. O. Hughes *et al.*, Small molecule SARM1 inhibitors recapitulate the SARM1−/− phenotype and allow recovery of a metastable pool of axons fated to degenerate. *Cell Rep.* **34**, 108588 (2021).
29. M. Giroud *et al.*, Discovery of a potent SARM1 base-exchange inhibitor with in vivo efficacy. *J. Med. Chem.* **68**, 6558–6575 (2025).
30. S. A. Green *et al.*, Optimization of brain penetrant SARM1 orthosteric inhibitors and discovery of their paradoxical subinhibitory activation. *ACS Med. Chem. Lett.* **16**, 1147–1154 (2025).
31. H. C. Feldman *et al.*, Selective inhibitors of SARM1 targeting an allosteric cysteine in the autoregulatory ARM domain. *Proc. Natl. Acad. Sci. U.S.A.* **119**, e2208457119 (2022).
32. M. Bratkowski *et al.*, Uncompetitive, adduct-forming SARM1 inhibitors are neuroprotective in preclinical models of nerve injury and disease. *Neuron* **110**, 3711–3726.e16 (2022).
33. L. Wang *et al.*, SARM1 senses dsDNA to promote NAD+ degradation and cell death. *Cell* **188**, 7137–7154.e21 (2025).
34. J. Gerdts, D. W. Summers, Y. Sasaki, A. DiAntonio, J. Milbrandt, Sarm1-mediated axon degeneration requires both SAM and TIR interactions. *J. Neurosci.* **33**, 13569–13580 (2013).
35. Y. Sasaki *et al.*, cADPR is a gene dosage-sensitive biomarker of SARM1 activity in healthy, compromised, and degenerating axons. *Exp. Neurol.* **329**, 113252 (2020).
36. W. H. Li *et al.*, Permeant fluorescent probes visualize the activation of SARM1 and uncover an anti-neurodegenerative drug candidate. *eLife* **10**, e67381 (2021).
37. D. Yu *et al.*, TIR domains of plant immune receptors are 2′, 3′-cAMP/cGMP synthetases mediating cell death. *Cell* **185**, 2370–2386.e18 (2022).
38. Y. Huang *et al.*, Stepwise activation of SARM1 for cell death and axon degeneration revealed by a biosynthetic NMN mimic. *Proc. Natl. Acad. Sci. U.S.A.* **122**, e2424906122 (2025).

Downloaded from https://www.pnas.org by 151.76.23.94 on September 13, 2026 from IP address 151.76.23.94.

39. C. Del Nagro, Y. Xiao, L. Rangell, M. Reichelt, T. O'Brien, Depletion of the central metabolite NAD leads to oncosis-mediated cell death. *J. Biol. Chem.* **289**, 35182–35192 (2014).
40. K. Huang *et al.*, Base-exchange enabling the visualization of SARM1 activities in sciatic nerve-injured mice. *ACS Sens.* **8**, 767–773 (2023).
41. T. Wu *et al.*, SARM1 executes neuronal parthanatos and promotes excitotoxic cell death. *Neuron* **114**, 2975–2986.e5 (2026).
42. S. Geisler, Augustus Waller's foresight realized: SARM1 in peripheral neuropathies. *Curr. Opin. Neurobiol.* **87**, 102884 (2024).
43. H. Murata *et al.*, c-Jun N-terminal kinase (JNK)-mediated phosphorylation of SARM1 regulates NAD+ cleavage activity to inhibit mitochondrial respiration. *J. Biol. Chem.* **293**, 18933–18943 (2018).
44. W. Yue *et al.*, Deubiquitination of SARM1 by USP13 regulates SARM1 activation and axon degeneration. *Life Med.* **2**, lnad040 (2023).
45. C. Chen *et al.*, Hyperglycemia promotes SIRT3-mediated deacetylation of SARM1 to exacerbate diabetic peripheral neuropathy in mice. *Proc. Natl. Acad. Sci. U.S.A.* **123**, e2517110123 (2026).
46. Y. Sasaki, B. P. S. Vohra, F. E. Lund, J. Milbrandt, Nicotinamide mononucleotide adenylyl transferase-mediated axonal protection requires enzymatic activity but not increased levels of neuronal nicotinamide adenine dinucleotide. *J. Neurosci.* **29**, 5525–5535 (2009).
47. F. W. Studier, Protein production by auto-induction in high-density shaking cultures. *Protein Expr. Purif.* **41**, 207–234 (2005).
48. M. Piotto, V. Saudek, V. Sklenář, Gradient-tailored excitation for single-quantum NMR spectroscopy of aqueous solutions. *J. Biomol. NMR* **2**, 661–665 (1992).
49. D. N. Mastronarde, Automated electron microscope tomography using robust prediction of specimen movements. *J. Struct. Biol.* **152**, 36–51 (2005).
50. A. Kao *et al.*, Dataset for 'Direct activation of SARM1 by dsDNA is not supported by biochemical and cellular evidence.' Digital Commons Data@Becker. https://doi.org/10.17632/js8prhg99r. Deposited 9 September 2026.

Downloaded from https://www.pnas.org by 151.76.23.94 on September 13, 2026 from IP address 151.76.23.94.